Ternary Metal-Rich Phosphides: Structure, Bonding, and Site Preferences in ZrNbP and $Hf_{1+x}Mo_{1-x}P$

Gordon J. Miller* and Jun Cheng

Department of Chemistry and Ames Laboratory/DOE, Iowa State University, Ames, Iowa 50011

Received November 10, 1994[⊗]

Semiempirical electronic structure calculations are utilized to assess the bonding and metal atom arrangement in the recently discovered ternary phosphide ZrNbP, which adopts the Co_2Si structure type. These same calculations reveal that ZrMoP should form in the Fe_2P structure type due primarily to metal−metal interactions within each system. Related structural alternatives like the Cu_2Sb-type and the Ni_2In-type are also examined for their stability ranges as a function of valence electron concentration (vec). Synthesis and structural characterization of $Hf_{1.06}Mo_{0.94}P$ by single-crystal X-ray diffraction are also reported and confirm the prediction of stability of the Fe_2P structure type for this vec. $Hf_{1.06}Mo_{0.94}P$ crystallizes in the space group $P\bar{6}2m$ (No. 189); a = 6.8954(4) Å; c = 3.4164(4) Å; Z = 3; R = 0.024; R_w = 0.027 ($I \geq 3\sigma(I)$).

The chemistry of transition metal-rich chalcogenides has been receiving increasing attention due to the fascinating structures and metal atom ordering phenomena among mixed-metal sulfides and selenides.[1] Ternary phosphides also comprise an important fundamental class of refractory compounds, but these generally involve the combination of an early transition metal (Zr, Nb, Mo) with a late transition metal, generally from the 3d series (Fe, Co, Ni).[2] Rarely have mixed early transition metal phosphides been isolated and structurally characterized.

The recent report of the Co_2Si structure type (C37-type from *Strukturbericht*; oP12[3]) for ZrNbP[4] is, perhaps, somewhat surprising, given that metal-rich compounds of this type generally form other, quite complex structure types, e.g., Zr_2P[5] (oC108) and Nb_2P[6] (oP54). These contain some metal atoms in local environments that are similar to a body-centered cubic (bcc) arrangement. Another surprising aspect of ZrNbP is the clear separation of Zr and Nb into different crystallographic sites with no evidence for mixed site occupations nor of any variable compositions, $Zr_{1\pm x}Nb_{1\mp x}P$. This compound differs from the (Ta, Nb) sulfides, in which there is an incomplete segregation of Nb and Ta atoms into inequivalent sites, but is similar to them in that these ternary sulfides occur only for specific Ta:Nb ratios.

In this article, we examine the electronic structure of the Co_2Si structure type using the metals Zr, Nb, and Mo with P in order to assess the electronic influences on metal segregation and minimal homogeneity width. We also address the preference of the Co_2Si structure over related structure types for compounds with valence electron concentrations (vec's) near ZrNbP. These calculations led to an investigation of more electron rich systems and the discovery of the Fe_2P-type structure in the (Hf,Mo)P system. The syntheses of these compounds and the single-crystal structural determination of $Hf_{1.06}Mo_{0.94}P$ will also be presented.

The Co_2Si Structure Type

Much has been written regarding the Co_2Si structure type.[7] Other designations include $PbCl_2$ (C23-type) and SrH_2 (C29-type), but Hyde et al.[7] recently pointed out that there should be no distinction between the C23- and C29-types. Each of these compounds adopts the same space group, *Pnma*, with three atoms in the asymmetric unit occupying 4*c* Wyckoff sites (x_i, $^1/_4$, z_i). However, differences in the ratios of the lattice constants a/b and c/b (b = shortest lattice parameter) indicate that these different designations are indeed appropriate to describe the flexibility allowed by the orthorhombic symmetry. Hulliger has also demonstrated the relationship between Co_2Si (C37) and Ni_2In ($B8_b$-type).[8]

Jeitschko,[9] Flahaut and Thévet,[10] and Hyde et al.[7] have independently constructed sorting diagrams using various lattice parameter ratios. Their results identify at least two primary regimes, although the "borders" are not well defined. Nevertheless, the Co_2Si (C37) regime corresponds to $1.80 \leq c/b \leq 2.20$ and $1.25 \leq a/b \leq 1.40$ whereas the $PbCl_2$ (C23) regime occurs for $1.60 \leq c/b \leq 2.50$ and $1.50 \leq a/b \leq 1.90$. Clearly, the a/b ratio is the significant parameter for this segregation. In general, the difference between the $PbCl_2$ and Co_2Si structure types is noted when the coordination numbers of the majority components in binary compounds are examined. In the $PbCl_2$ structure, these coordination numbers are unequivocally 4 (tetrahedral) and 5 (square pyramidal) whereas, in the Co_2Si structure, these values tend to increase by the addition of capping atoms: i.e., the coordination polyhedra resemble trigonal bipyramids and octahedra. In the Ni_2In ($B8_b$) structure, this trend is completed with the coordination numbers 5 (trigonal bipyramidal) and 6

[⊗] Abstract published in *Advance ACS Abstracts*, May 1, 1995.

(1) (a) Harbrecht, B.; Franzen, H. F. *Z. Anorg. Allg. Chem.* **1987**, *551*, 74. (b) Harbrecht, B. *Z. Kristallogr.* **1988**, *182*, 118. (c) Harbrecht, B.; Franzen, H. F. *Z. Kristallogr.* **1989**, *186*, 119. (d) Yao, X.; Franzen, H. F. *J. Less-Common Met.* **1990**, *161*, L37. (e) Yao, X.; Franzen, H. F. *J. Solid State Chem.* **1990**, *86*, 88. (f) Yao, X.; Franzen, H. F. *Z. Anorg. Allg. Chem.* **1991**, *598*, 353. (g) Yao, X.; Franzen, H. F. *J. Am. Chem. Soc.* **1991**, *113*, 1426. (h) Yao, X.; Miller G. J.; Franzen, H. F.; *J. Alloys Comp.* **1992**, *183*, 7.

(2) Villars, P.; Calvert, L. D. *Pearson's Handbook of Crystallographic Data for Intermetallic Phases*; American Society for Metals: Metals Park, OH, 1985; Vol 3.

(3) This notation is called the Pearson symbol: oP12 means orthorhombic crystal class, Primitive unit cell setting, 12 atoms in the unit cell. See: Pearson, W. B. *Crystal Chemistry and Physics of Metals and Alloys*; Wiley: New York, 1972.

(4) Marking, G.; Franzen, H. F. *J. Alloys Comp.* **1994**, *204*, L16.

(5) Ahlzén, P.-J.; Rundqvist, S. *Z. Kristallogr.* **1989**, *189*, 117.

(6) Kuzma, Yu. B.; Orishchin, S. V.; Lomnitskaya, Ya. F., Glov'jak, T. *Dopov. Akad. Nauk Ukr. RSR, Ser. B: Geol., Khim. Biol. Nauki* **1988**, 47.

(7) (a) Hyde, B. G.; Andersson, S. *Inorganic Crystal Structures*; Wiley-Interscience: New York, 1989. (b) Hyde, B. G.; O'Keeffe, M.; Lyttle, W. M.; Brese, N. E. *Acta Chem. Scand.* **1992**, *46*, 216.

(8) Hulliger, F. *Struct. Bonding* **1968**, *4*, 83.

(9) Jeitschko, W. *Acta Crystallogr. Sect. B* **1968**, *B24*, 930.

(10) Flahaut, J.; Thévet, F. *J. Solid State Chem.* **1979**, *32*, 365.

0020-1669/95/1334-2962$09.00/0

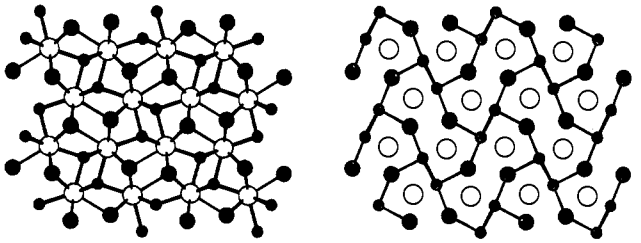

Figure 1. (001) projections of the Co_2Si structure type for ZrNbP: large open circles, P; small dark circles, Nb; midsized dark circles, Zr. (Left) Metal−phosphorus contacts are shown. (Right) Metal−metal contacts are shown.

(octahedral). With regard to chemical bonding interactions in these compound classes, the $PbCl_2$-type typically has weak interactions between the majority-component atoms, e.g., van der Waals Cl···Cl interactions, while the Co_2Si-type shows stronger polar covalent (or metallic) interactions between these two sets of atoms, especially if the internuclear distances are examined. Surprisingly, ZrNbP with $a/b = 1.928$ and $c/b = 2.339$ falls in the $PbCl_2$ regime (lower Zr and Nb coordination by P) and not the Co_2Si regime (presumably "stronger" Zr−Nb interactions).

Figure 1 illustrates two (010) projections of ZrNbP, one of which emphasizes the metal−phosphorus close contacts ("bonds") and the other of which shows the metal−metal interactions. In this and other related figures, P atoms are the large open circles, Nb atoms are the small dark circles, and Zr atoms are midsized dark circles. Zr and Nb segregate into two crystallographically inequivalent sites: Nb is tetrahedrally coordinated by P; Zr is square pyramidally coordinated by P. The shortest metal−metal contacts occur between adjacent Nb atoms as we identify a chain of edge-sharing $[NbP_4]$ tetrahedra (**1**). The connectivity of these

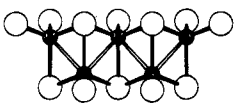

1

tetrahedra leads to a zigzag chain of Nb atoms, unlike the topologically related chain, **2**, that is observed for $^1_\infty[FeS_2]^-$ in

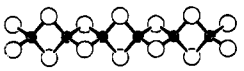

2

$KFeS_2$.[11] The second closest metal−metal contact occurs between Nb and Zr atoms as each $[NbP_4]$ tetrahedron shares two edges with two $[ZrP_5]$ square pyramids (the shared edge in the square pyramid is formed by one basal P atom and the axial P atom). This mode of polyhedral condensation forms zigzag Zr−Nb chains as well; see **3**.

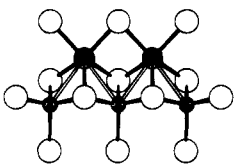

3

Thus, ZrNbP presents a dilemma in terms of structural classification. On the one hand, it belongs to the $PbCl_2$-type regime on the structural sorting diagram; on the other, the observed metal−metal distances indicate significant metal−metal bonding, which would be typical for Co_2Si-type structures.

(11) Boon, J. W.; MacGillavry, C. H. *Recl. Trav. Chim. Pays-Bas* **1942**, *61*, 910.

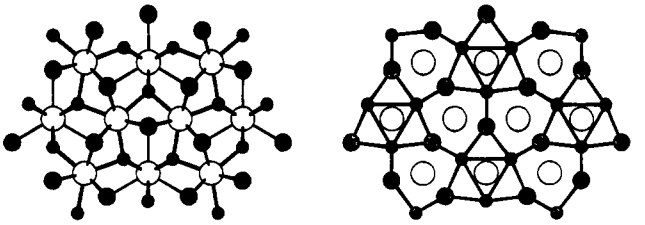

Figure 2. (001) projections of the Fe_2P structure type for a hypothetical ZrNbP. The same conventions as in Figure 1 are used.

Related Structural Alternatives

As we have already mentioned, the Co_2Si structure type is closely related to the hexagonal Ni_2In structure, which is itself a ternary derivative of the AlB_2 (C32-type).[3,7a] In this structure, one Ni atom and the In atom form alternant honeycomb (6^3) sheets stacked in an eclipsed, yet alternating, fashion, with the additional Ni atoms occupying the centers of every hexagonal prism. If we constructed ZrNbP in the Ni_2In structure, one of the metal atoms would be octahedrally coordinated by P, while the other (the one in the honeycomb nets) would be coordinated by a trigonal bipyramid of P atoms.

If we concentrate on the coordination environments for Nb and Zr in ZrNbP, then we can identify two alternative structures that allow four-coordinate tetrahedral Nb atoms and five-coordinate square pyramidal Zr atoms: (i) the Fe_2P-type;[3,7a] and (ii) the Cu_2Sb-type.[3,7a] In hexagonal Fe_2P, three $[FeP_4]$ tetrahedra are condensed via common edges to form Fe_3 triangles (**4**). Figure 2 illustrates (001) projections of Fe_2P, and

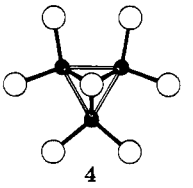

4

as in Figure 1, we show two types of connectivities: (1) metal−phosphorus and (2) metal−metal contacts. The shortest metal−metal distances occur between the two symmetry-inequivalent sites and form zigzag chains. If the coordination environment is included, we note that the $[MP_5]$ square pyramids are condensed via *trans*-basal edges to form a chain, and these shared edges also form an edge of each $[M'P_4]$ tetrahedron; see **5**.

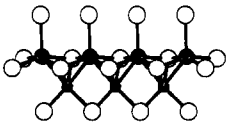

5

Figure 3 shows a skew (100) projection of the Cu_2Sb structure type using the same convention as in the other illustrations. Cu_2Sb adopts a tetragonal crystal class, space group *P4/nmm*, and, perhaps, can be succinctly described as an intergrowth between anti-PbO-type and NaCl(001)-type sheets.[7a] In terms of potential metal−metal interactions, the two-dimensional layer of edge-sharing tetrahedra (anti-PbO) provides a square net of metal atoms. There are no other short (less than 3.30 Å) metal−metal interactions in this case.

We should point out a few additional relationships among these four structure types: Co_2Si; Ni_2In; Fe_2P; Cu_2Sb. The

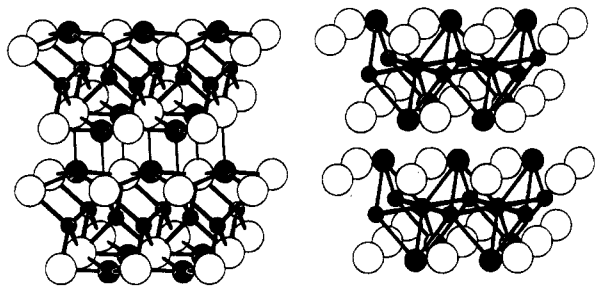

Figure 3. Skewed (100) projections of the Cu_2Sb structure type for a hypothetical ZrNbP. The same conventions as in Figure 1 are used.

metal atoms in the Fe_2P-type, as in Co_2Si, can be shifted to positions that center P octahedra and trigonal bipyramids. However, such shifts would create lower symmetry coordination polyhedra for the metal atoms by adjacent metals, which are unobserved. Furthermore, the five-coordinate metal atom in Co_2Si, Fe_2P, and Cu_2Sb also has a sixth ligand at a slightly extended distance (by a factor of nearly 15%) from the metal, but in a position of the vacant site for ideal octahedral coordination.

We detail these structural features because, in the subsequent sections, we describe how the electronic structures of these various alternatives influence the stability of these various structures, as well as the crystal chemistry of the observed phases.

Structural Preferences: Theory

A recent development within the semiempirical Hückel theory,[12] in particular, the concept of second moments scaling,[13] shows extremely high success in accounting for different topologies for most of the elements as well as for a diverse collection of binary compounds.[14] This method involves evaluating the second moments of the densities of electronic states (DOS) for every structure under consideration and then scaling the DOS curves until the second moment for each structure adopts the same value. The second moment μ_2 for a continuous distribution of electronic states $\varrho(E)$ is defined by $\mu_2 = \int_{-\infty}^{\infty} E^2\, \varrho(E)\, dE$. Within the LCAO approximation, construction of the $(N \times N)$ Hamiltonian matrix (N is the number of AO's in the unit cell) allows another expression of the second moment:

$$\mu_2 = \sum_{i=1}^{N} (H_{ii})^2 + \sum_{i,j=1}^{N} H_{ij}H_{ji}$$

At present, all investigations have considered homonuclear models, that is, elemental structures or the electronegative network in a binary compound, whether it be a salt or intermetallic. Within a homonuclear system, the diagonal Hamiltonian matrix elements, the H_{ii} values, do not affect the scaling procedure. However, for heteronuclear systems, comparison can only be performed between compounds having identical stochiometries in order to maintain equal $\sum(H_{ii})^2$ values from one structure to the other. Within identical stoichiometries, the scaling procedure involves $\sum H_{ij}H_{ji}$, the same expression as for homonuclear systems.

(12) (a) Hoffmann, R.; Lipscomb, W. N. *J. Chem. Phys.* **1962**, *36*, 2179, 3489. (b) Hoffmann, R. *J. Chem. Phys.* **1963**, *39*, 1397. (c) Ammeter, J. H.; Bürgi, H.-B.; Thibeault, J. C.; Hoffmann, R. *J. Am. Chem. Soc.* **1978**, *100*, 3686.

(13) Lee, S. *Acc. Chem. Res.* **1991**, *24*, 249.

(14) (a) Lee, S. *J. Am. Chem. Soc.* **1991**, *113*, 101. (b) Hoistad, L. M.; Lee, S. *J. Am. Chem. Soc.* **1991**, *113*, 8216. (c) Hoistad, L. M.; Lee, S.; Pasternak, J. *J. Am. Chem. Soc.* **1992**, *114*, 4790.

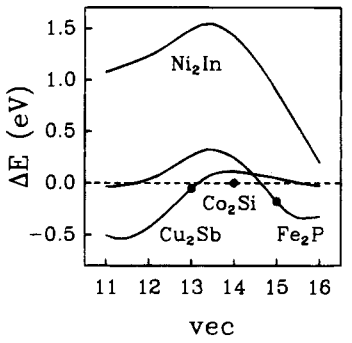

Figure 4. Energy difference curves vs vec for the four structure models of ZrNbP. The baseline ($\Delta E = 0$) is for the Co_2Si-type.

Table 1. Structural Details of Various MM'P Models of ZrNbP: M ≡ Zr; M' ≡ Nb

	MM'P			
	Co_2Si	Fe_2P	Cu_2Sb	Ni_2In
space group	*Pnma*	*P*$\bar{6}$*2m*	*P4/nmm*	*P6*$_3$*/mmc*
Lattice params, Å				
a	6.890	7.051	3.821	4.513
b	3.573			
c	8.358	3.571	7.097	5.220
bond distances < 3.3 Å				
M'−P	2.554 (2×)	2.554 (2×)	2.605 (4×)	2.605 (3×)
	2.622 (1×)	2.651 (2×)		2.610 (2×)
	2.692 (1×)			
M−P	2.717 (2×)	2.750 (4×)	2.750 (4×)	2.914 (6×)
	2.769 (2×)	3.042 (1×)	3.042 (1×)	
	3.042 (2×)			
M'−M'	2.816 (2×)	3.163 (2×)	2.702 (4×)	
M'−M	3.014 (2×)	2.820 (2×)	2.978 (4×)	2.914 (6×)
	3.122 (2×)	3.197 (4×)		
M−M				

For the dimetal phosphides, the shortest distances occur between metals and phosphorus. If we also consider the charge transfer that occurs in these bonds as well as the relative size of the individual atomic orbitals, the metal−phosphorus interactions are correspondingly greater than the metal−metal interactions. In terms of second moment scaling, we have selected models of the Fe_2P-, Cu_2Sb-, and Ni_2In-type structures using ZrNbP in which the metal−phosphorus environments satisfy a constant value of $\sum H_{ij}H_{ji}$, i.e., the value for the reported Co_2Si-type structure.[4] Table 1 lists various structural parameters of these four structure models of ZrNbP. The Appendix describes the computational details. Figure 4 shows three energy difference curves with the baseline ($\Delta E = 0$) corresponding to the Co_2Si structure of ZrNbP. The lowest line for a given vec represents the most electronically stable structure at that electron count.

Regarding the observed structure of ZrNbP, these curves are remarkably accurate. The curves also predict that, for counts greater than 14 per formula unit, the Fe_2P structure type becomes favorable, while for counts less than 14 per formula unit, the Cu_2Sb-type becomes competitive. A wide range of unit cell sizes for the Ni_2In-type showed this to be an unfavorable structure for ZrNbP except under significant compression. Therefore, under hydrostatic pressure, ZrNbP is a candidate for a structural phase transformation from Co_2Si-type (*Pnma*) to Ni_2In-type (*P6*$_3$*/mmc*).

$Hf_{1.06}Mo_{0.94}P$: The Fe_2P Structure Type Occurs!

In an effort to pursue some of the predictions of Figure 4, we have carried the successful synthesis and structural characterization of $Hf_{1.06}Mo_{0.94}P$.

Table 2. Structure Determination Summary for $Hf_{1.06}Mo_{0.93}P$

space group	$P\bar{6}2m$ (No. 189)
unit cell dimens	$a = 6.886(2)$ Å
	$c = 3.410(1)$ Å
volume	140.03(8) Å^3
Z	3
density (calc)	11.040 Mg/m^3
crystal size (mm)	0.08 × 0.03 × 0.03
abs coeff	64.885 mm^{-1}
radiation	Mo Kα ($\lambda = 0.710\ 73$ Å)
temp	296(1) K
2θ range	3.0−60.1°
scan range (ω−2θ)	$(1.26 + 0.30 \tan\theta)°$
scan speed	8.0°/min in ω
index ranges	$-10 \le h \le 10, 0 \le k \le 10, -5 \le l \le 5$
no. of reflns collected	622
no. of independent reflns	181 ($R_{int} = 0.061$)
no. of obsd reflns	165 ($F_o^2 \ge 3\sigma(F_o^2)$)
no. of min/max transm	0.67/1.00
extinction corr	2.66×10^{-6}
weighting scheme	$w = 1/\sigma^2(F_o^2)$
no. of params refined	15
R indices [$F_o^2 \ge 3\sigma(F_o)$]	$R^a = 0.026$, $R_w{}^b = 0.026$
GooF[c]	1.82
data-to-param ratio	11.0:1
largest diff peak	2.61 e Å^{-3}
largest diff hole	−2.25 e Å^{-3}

$^a R = \sum||F_o| - |F_c||/\sum|F_o|$. $^b R_w = [\sum w(|F_o| - |F_c|)^2/\sum w|F_o|^2]^{1/2}$. ^{c} GooF $= \sum[(|F_o| - |F_c|)/\sigma(|F_o|)]/(N_{obs} - N_{par})$.

Synthesis. A sample of $Hf_{1.06}Mo_{0.94}P$ was prepared from a 1:1 molar mixture of Mo powder (Alfa; − 200 mesh, 99.9%) and HfP (prepared from Hf files (Alfa; 99.99%) and red phosphorus (Alfa; −100 mesh, 99%) in an evacuated fused silica ampule that was heated slowly to 1073 K). This mixture was arc-melted (10 V, 60 A) for 30 s under an Ar atmosphere on a water-cooled copper hearth. The pellet was subsequently inverted and arc-melted twice more to promote homogenization. The total weight loss after arc-melting was less than 4%.

Structure Determination. An X-ray powder diffraction pattern, taken on an Enraf-Nonius Guinier camera using monochromatized Cu $K\alpha_1$ radiation and NBS Si powder as an internal standard, showed 18 sharp reflections (20° < 2θ < 80°) that could be indexed with the program TREOR to give a hexagonal lattice with $a = 6.8954(4)$ Å and $c = 3.4164(4)$ Å.

The arc-melted sample was then annealed in an induction furnace at approximately 1873 K for 5 h with a residual pressure less than 10^{-7} Torr. The sample was partially melted, and small orthorhombic crystals that were suitable for single-crystal X-ray diffraction could be picked from the crushed sample. A silvery needle-shaped crystal was mounted on a glass rod in air. The cell parameters of the single crystal were determined by least-squares analysis of 15 reflections (14.8° < 2θ < 30.8°) centered on a Rigaku AFC6 rotating-anode diffractometer with monochromatized Mo Kα radiation. The data collection proceeded at room temperature using the ω−2θ mode with $2\theta \le 60°$. The measured intensities were corrected for Lorentz and polarization and absorption effects (using an empirical correction), and the final least-squares lattice parameters were calculated from Guinier X-ray powder patterns of the bulk sample. Crystallographic details are listed in Table 2.

The structure was solved using the Fe_2P structure type as a model, space group $P\bar{6}2m$, which is characterized by no systematic absences. An initial model, in which Mo and Hf were completely segregated on Wyckoff positions 3*f* and 3*g*, respectively, could be refined with isotropic displacement parameters to the residuals $R = 0.031$ and $R_w = 0.034$ using TEXSAN software.[15] However, the 3*f* site gave a nonpositive definite displacement parameter. Therefore, Hf and Mo were assigned to the 3*f* site under the constraint SOF(Hf(2)) + SOF(Mo) = 1, and their displacement parameters, both isotropic and anisotropic, were set equal to one another. We found best refinement ($R = 0.026$; $R_w = 0.026$) for 6.4(3)% Hf on the 3*f* site and well-behaved anisotropic displacement parameters. Figure 5 illustrates a (001) projection of $Hf_{1.06}Mo_{0.94}P$ showing 99% thermal ellipsoids. Table 3 lists the positional and displacement parameters, and Table 4 contains some selected bond lengths for $Hf_{1.06}Mo_{0.94}P$. Atomic scattering factors and anomalous dispersion corrections were taken from ref 16. (A complete listing of the crystallographic data may be obtained as supplementary material from the authors.)

(15) TEXSAN, TEXRAY Structure Analysis Package, Molecular Structure Corp., 1985.

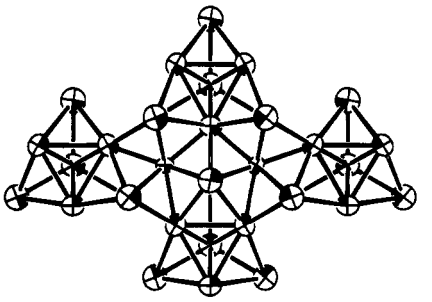

Figure 5. (001) projections of the Fe_2P-type structure of $Hf_{1.06}Mo_{0.93}P$. Contacts less than 3.10 Å are indicated; the heavier lines are metal−phosphorus contacts; the lighter lines are metal−metal contacts. 99% thermal ellipsoids are represented.

Table 3. Positional and Equivalent Isotropic Displacement Parameters for $Hf_{1.06}Mo_{0.93}P$

atom	site	x	y	z	SOF	U_{eq}, Å
Hf(1)	3*g*	0.5961(2)	0	1/2	1	0.075(4)
Hf(2)	3*f*	0.2527(3)	0	0	0.064(3)	0.062(10)
Mo	3*f*	0.2527(3)	0	0	0.936(3)	0.062(10)
P(1)	1*b*	0	0	1/2	1	0.071(18)
P(2)	2*c*	1/3	2/3	0	1	0.050(6)

Table 4. Selected Bond Distances (Å) in $Hf_{1.06}Mo_{0.93}P$ (M(2) = Hf(2) and Mo)

Hf(1)−P(1)	2.780(1), 1×	Hf(1)−P(2)	2.702(1), 4×
Hf(1)−M(2)	2.915(2), 2×	Hf(1)−M(2)	2.971(1), 4×
Hf(1)−Hf(1)	3.410(1), 2×	Hf(1)−Hf(1)	3.629(1), 4×
M(2)−P(1)	2.437(1), 2×	M(2)−P(2)	2.617(1), 2×
M(2)−M(2)	3.015(3), 2×	M(2)−M(2)	3.410(1), 2×

Phase Widths. Preliminary attempts to probe the range of homogeneity in $Hf_{1+x}Mo_{1-x}P$ suggest that the Fe_2P structure type occurs for $-0.33 \le x \le 0.25$, i.e., "$Hf_{0.67}Mo_{1.33}P$" to "$Hf_{1.22}Mo_{0.78}P$". Guinier X-ray powder diffraction indicate that the unit cell volumes increase from 140.09(2) Å^3 ($x = -0.33$) to 141.12(3) Å^3 ($x = 0.22$). On the other hand, ZrNbP does *not* show a corresponding range of homogeneity.

Discussion

Although the total energies obtained with the semiempirical electronic structure calculations provided agreement with the observation of the Co_2Si structure for ZrNbP and the Fe_2P structure for $Hf_{1.06}Mo_{0.94}P$, we need to examine the DOS curves and crystal orbital overlap populations (COOPs)[17] of the various alternatives in order to accurately assess rationale of structural preferences in terms of chemical bonding arguments. Figure 6 illustrates the total DOS curves calculated for ZrNbP in the four structure types. In all cases, for reasons we shall address shortly, the Nb atoms occupy the sites with lower P coordination, and Zr, the sites with higher P coordination. With regard to metal−phosphorus interactions, all four DOS curves are similar, with the band between −16 and −12 eV identified as mostly P 3p and metal−phosphorus bonding. The dispersion within the

(16) *International Tables for X-Ray Crystallography*; Kynoch: Birmingham, England, 1992; Vol. C.

(17) (a) Hughbanks, T.; Hoffmann, R. *J. Am. Chem. Soc.* **1983**, *105*, 3528. (b) Wijeyesekera, S. D.; Hoffmann, R. *Organometallics* **1984**, *3*, 949. Ammeter, J. H.; Bürgi, H.-B.; Thibeault, J. C.; Hoffmann, R. *J. Am. Chem. Soc.* **1978**, *100*, 3686.

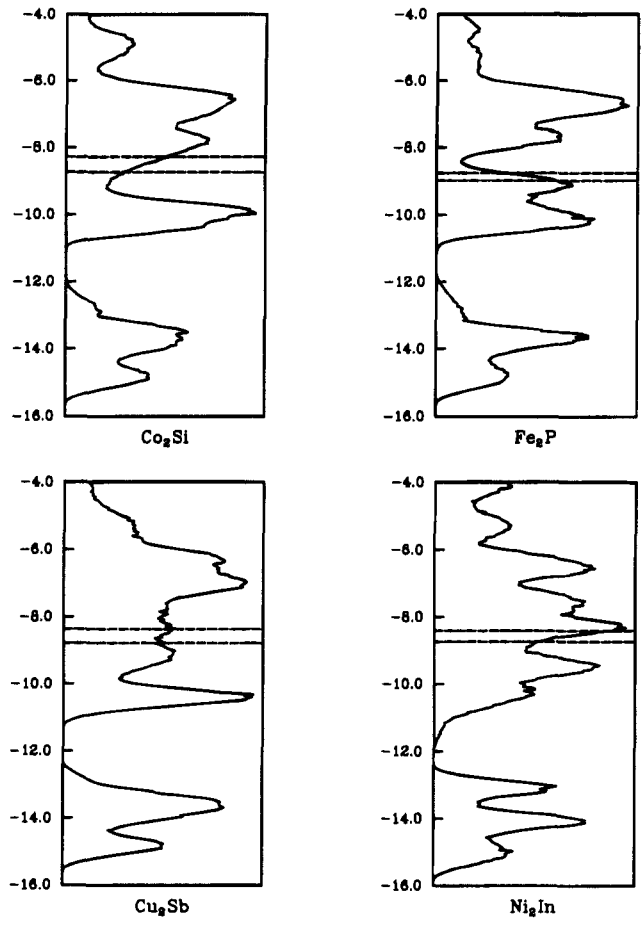

Figure 6. Total DOS curves for various structural models of ZrNbP: Co_2Si-type, Fe_2P-type; Cu_2Sb-type; Ni_2In-type. Lower dashed line is E_F (vec = 14); higher dashed line is E_F (vec = 15).

conduction band ($E > -11$ eV) is largely due to direct metal–metal interactions and is mildly affected by through-bond metal–metal coupling via bridging P atoms. Clearly, the conduction bands in the Co_2Si and Fe_2P models show structures that suggest significant metal–metal bonding: there are sharp minima in the DOS near −9.0 eV (Co_2Si) and −8.3 eV (Fe_2P). The positions of these band minima relative to E_F for vec values of 14 and 15 follow the energy difference curves in Figure 4: the Co_2Si-type is preferred for vec ≤ 14; the Fe_2P-type is preferred for vec ≥ 15. The Cu_2Sb model also has a low-lying metal–metal bonding band, but this integrates to just two electrons per metal; i.e., vec = 12. Finally, the Ni_2In-type has a broader conduction band ($E_{min} \sim 12.0$ eV), but most of its character lies above −10.0 eV. We shall assign orbital character to these bands by evaluating their COOPs.

We addressed the site preference problem of the different metals by performing a Mulliken population analysis on model M_2P systems in which the two metal atoms are chosen to be identical. Due to metal–phosphorus and metal–metal bonding interactions, the total population arises from orbital overlap in these two types of bonds as well as the charge transfer taking place. The rule of topological charge stabilization[18] allows assessment of structures of ternary derivatives by hypothesizing that the more electronegative atom will occupy the site with the larger Mulliken population in the model M_2P systems. On any electronegativity scale, $\chi(Nb) > \chi(Zr)$, or in general, among the group 4–6 metals, electronegativity increases with group number. Our calculations show that, in the Co_2Si arrangement,

(18) (a) Gimarc, B. M. *J. Am. Chem. Soc.* **1983**, *105*, 1979. (b) Burdett, J. K. *Prog. Solid State Chem.* **1984**, *15*, 173.

Table 5. Computational Results on Four MM'P Models for Different vec Values (M = Zr Parameters; M' = Nb Parameters)[a]

	MM'P			
	Co_2Si	Fe_2P	Cu_2Sb	Ni_2In
		vec = 13		
E_F, eV	−9.484	−9.259	−9.111	−9.065
$\langle E \rangle$, eV	0.000[a]	0.268	−0.154	0.692
q(M')	4.560	4.433	4.496	4.234
q(M)	2.901	3.028	2.926	3.279
q(P)	5.539	5.539	5.578	5.487
p(M'–P)	0.247	0.240	0.209	0.217
p(M–P)	0.194	0.159	0.181	0.097
p(M'–M')	0.194	0.135	0.209	
p(M'–M)	0.181	0.143	0.134	0.118
		vec = 14		
E_F, eV	−8.728	−9.005	−8.774	−8.886
$\langle E \rangle$, eV	0.000[a]	0.247	0.016	0.828
q(M')	5.131	5.197	4.940	4.840
q(M)	3.315	3.248	3.466	3.655
q(P)	5.554	5.555	5.594	5.505
p(M'–P)	0.245	0.239	0.205	0.190
p(M–P)	0.195	0.160	0.183	0.096
p(M'–M')	0.188	0.123	0.210	
p(M'–M)	0.212	0.155	0.138	0.127
		vec = 15		
E_F, eV	−8.274	−8.751	−8.365	−8.679
$\langle E \rangle$	0.000[a]	−0.178	−0.052	0.527
q(M')	5.687	5.960	5.466	5.558
q(M)	3.739	3.470	3.922	3.920
q(P)	5.574	5.570	5.612	5.522
p(M'–P)	0.241	0.237	0.200	0.189
p(M–P)	0.197	0.161	0.187	0.095
p(M'–M')	0.176	0.109	0.214	
p(M'–M)	0.203	0.168	0.147	0.136

[a] $\langle E \rangle$ values are referenced to the Co_2Si-type.

the difference in Mulliken populations ($\Delta q = q$(tet) − q(sq pyr)) between the two metal sites for vec = 14 is 0.54 and, in the Fe_2P arrangement for vec = 15, the corresponding difference is 0.81. These results corroborate the strong segregation of Zr and Nb in ZrNbP and of Hf and Mo in $Hf_{1+x}Mo_{1-x}P$. In earlier work on $Nb_xTa_{2-x}S$,[1h] a similar Mulliken analysis for the two symmetry-inequivalent metal atom sites gave $\Delta q = 0.15$. For $Nb_{0.95}Ta_{1.05}S$, these two site are significantly populated by Nb and Ta: M1 (lower S coordination) is 77% Ta, 23% Nb; M2 (higher S coordination) is 28% Ta, 72% Nb.

Table 5 summarizes some of the important quantitative information obtained from these calculations for vec values of 13, 14 (ZrNbP), and 15 (HfMoP). For all vec values, the degree of charge transfer from metal to phosphorus among the four structure types increases from Ni_2In through both Co_2Si and Fe_2P to the Cu_2Sb structure type. This result parallels, in general, the observed pnictide compounds adopting these structures.[2] Thus, the subtle differences between the Co_2Si and Fe_2P types occur through the metal–metal interactions. Examination of Table 5 for metal–metal overlap populations in these two models shows the strongest interactions to occur, in general, between neighboring Nb atoms and between neighboring Nb and Zr atoms with distances less that 3.20 Å. In the Co_2Si structure, these are zigzag chains of Nb atoms (**1**) and two different chains of alternating Nb–Zr contacts (**3** illustrates one type of chain). In the Fe_2P structure, the heteronuclear metal–metal contacts (**5**) are stronger than the homonuclear interactions. Figure 7 shows the COOP curves for these four sets of bonds with Fermi levels indicated for ZrNbP in the Co_2Si-type and "ZrMoP" in the Fe_2P-type. Clearly, we see that, for each structure type, the heteronuclear interactions are

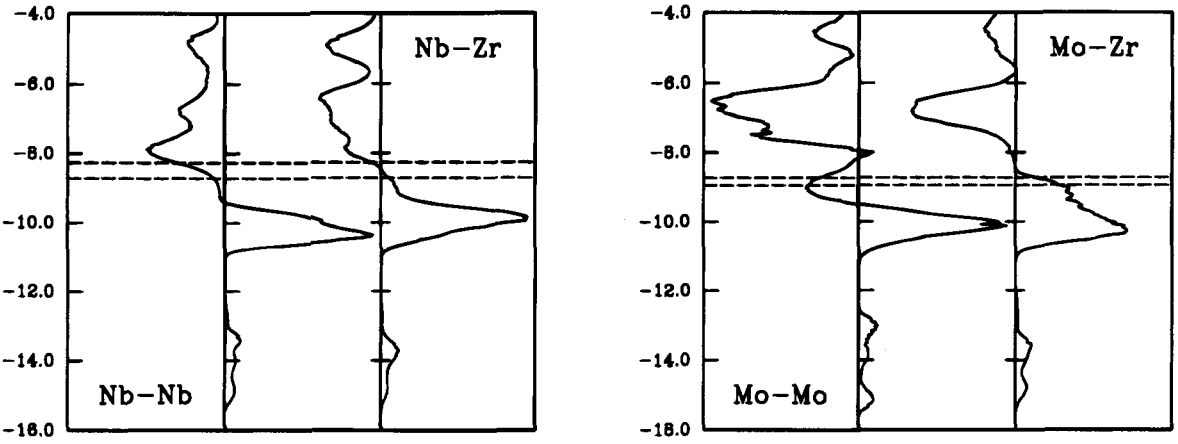

Figure 7. COOP curves for the shortest metal−metal contacts in two models of ZrNbP: (left) Co_2Si-type (observed structure); (right) Fe_2P-type (observed for $Hf_{1+x}Mo_{1-x}P$).

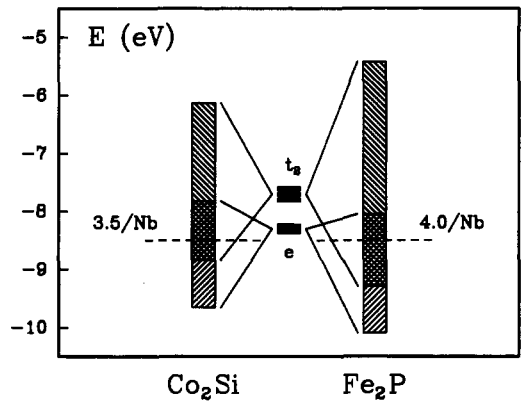

Figure 8. Broadening of the M′ (Nb parameters) orbitals from an isolated $[M'P_4]$ tetrahedron into the two different modes of condensed tetrahedra observed in the Co_2Si-type (ZrNbP) and Fe_2P-type (HfMoP). Dashed lines indicate the positions of maximum M′−M′ bonding in these fragments and are marked for the number of d electrons per M′ atom.

optimized (the Fermi level E_F occurs at the energy where the overlap population for these contacts crosses from bonding to antibonding), while the natures of the homonuclear Nb−Nb or "Mo−Mo" orbital overlaps differ. In ZrNbP, the Nb−Nb interaction is essentially maximized with the Fermi level lying at the top of a region of Nb−Nb nonbonding (weakly antibonding) orbitals. However, in "ZrMoP", there is significant "Mo−Mo" antibonding interaction within the triangular "clusters" at the Fermi level. These features of the metal−metal bonding in these compounds are well demonstrated by the bond distances in the observed compounds ZrNbP and $Hf_{1.06}Mo_{0.93}P$. Note that the single-bond metallic radii of Zr (1.454 Å) and Hf (1.442 Å) are nearly identical due to relativistic effects on the valence electrons in Hf. The distances are as follows: for ZrNbP, d(Nb−Nb) = 2.816 Å, d(Zr−Nb) = 3.014 Å; for $Hf_{1.06}Mo_{0.93}P$, d(Mo−Mo) = 3.015 Å, d(Hf−Mo) = 2.915 Å. Note that the heteronuclear contacts follow the differences in metallic radii (Nb, 1.342 Å; Mo, 1.296 Å), whereas the significantly larger Mo−Mo distance indicates some antibonding character in these bonds.

Can we understand the behavior in the DOS and COOP curves for the Co_2Si and Fe_2P models for ZrNbP from a molecular viewpoint? In order to address this question, we have isolated certain important fragments from these two solid state structures. Figure 8 shows how the M′ levels of a $[M'P_4]$ (M′ = Nb) tetrahedron broaden into bands when they form either the chain of triangular clusters (**6**) observed for Mo atoms in $Hf_{1+x}Mo_{1-x}P$ or the zigzag chain of Nb atoms in ZrNbP[3] (**1**).

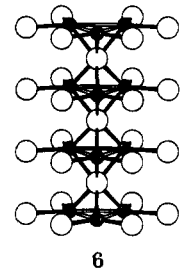

6

The phosphorus ligand field splits the M′ d orbitals into the doubly degenerate e level and the triply degenerate t_2 level. When M′−M′ orbital overlap is activated, both discrete levels are broadened via metal−metal bonding and antibonding interactions. The chains from the Fe_2P-type show a greater dispersion due to the (2+2) coordination of M′ atoms (2 within a triangular "cluster" and 2 along the c axis, but at about 15% longer distance). The figure also shows the energy values for each fragment (these are very nearly equal) below which the M′−M′ overlap is bonding and above which it is antibonding. Note that these levels occur for different vec values of the M′ atom and that both the e and t_2 bands are intersected. Analysis of the individual orbital populations shows that the M′ atoms in these structures have "configurations" of $(e)^{2.14}(t_2)^{1.36}$ (Co_2Si) and $(e)^{2.10}(t_2)^{1.90}$ (Fe_2P). Thus, the triangular arrangement allows for a greater population of levels derived from the t_2 orbitals that are *still* M′−M′ bonding. From the two structural models, the zigzag chain has three phosphorus atoms per M′ shared among three M′ atoms, whereas the triangle only has two phosphorus atoms shared among three M′ atoms. Therefore, there is a greater degree of M′−P−M′ through-bond coupling in the Co_2Si-type than in the Fe_2P-type, and this accounts for optimal M′−M′ bonding at lower vec values in the Co_2Si-type as well. However, this model neglects the effect of the M d orbitals on the overall pattern. The M′−M′ COOP curves in Figure 7 show that these interactions are slightly perturbed in the Co_2Si-type (ZrNbP) but are significantly affected in "ZrMoP" (Fe_2P-type). Evidently, the Co_2Si structure for ZrNbP offers the ability to optimize both Nb−Nb and Nb−Zr interactions. However, in "ZrMoP", there is some Mo−Mo antibonding character at the Fermi level.

We can use these results to hypothesize why the Co_2Si-type shows no homogeneity width around ZrNbP, whereas the Fe_2P-type does around HfMoP. The analysis of homonuclear vs heteronuclear metal−metal interactions in these two materials reveals more effective homonuclear Nb−Nb interactions in ZrNbP than between Mo atoms in HfMoP. In an effort to reduce the antibonding interactions between Mo atoms, Hf atoms

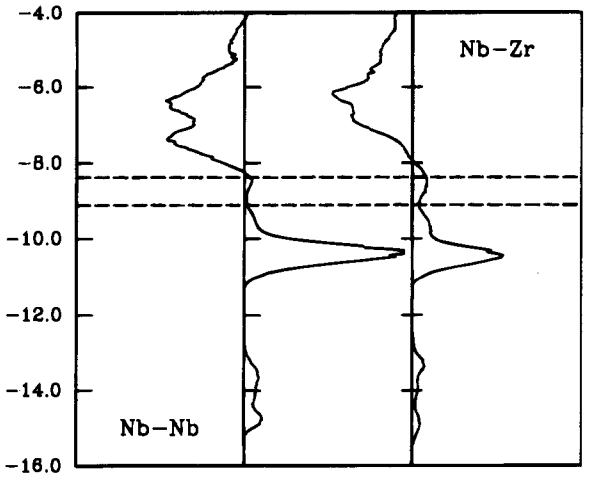

Figure 9. COOP curves for the shortest metal−metal contacts in the Cu_2Sb structure model for ZrNbP.

substitute for Mo and lower the Fermi level. Obviously, the subsequent "heteronuclear" interactions would be reduced by the depletion of electrons from bonding orbitals. A more subtle effect observed in the heteronuclear COOP curves is that the change from bonding to antibonding levels as energy increases is greater for the Co_2Si structure than for the Fe_2P structure. Therefore, HfMoP could raise its vec by replacing Hf by Mo without encountering strong antibonding interactions within the heteronuclear bonds. This is not the case for ZrNbP. Therefore, ZrNbP shows essentially no detectable homogeneity width, although our model does not preclude the possibility of a slight excess of Zr, i.e., $Zr_{1+x}Nb_{1-x}P$, whereas HfMoP tolerates a broader range of Hf:Mo ratios, as is observed.

We conclude this section with a few remarks about the Cu_2Sb structure type. In the realm of these early transition metal phosphides, our calculations suggest that such structures may be observed for vec below 14 per formula unit. Indeed, candidates would include YNbP, HfTiP, or perhaps even SrMoP, although Mo(I) is an unlikely electronic situation for Mo. Indeed, NaMnP[19] is characterized with this structure with Mn occupying the M′ sites (square net; tetrahedrally coordinated metal atoms). However, the greater metal-to-phosphorus charge transfer observed in our calculations may preclude observation of this structure type for this class of phosphides. Certainly, as Figure 9 illustrates, M′−M′ and M−M′ bonding is not optimized for these lower electron counts but occurs for vec = 15, where the Fe_2P structure is energetically competitive.

Summary

Rarely have semiempirical calculations predicted the structures of new compounds. Using the method of second moment scaling to structures that are related to the Co_2Si structure type of ZrNbP, we showed the Fe_2P structure to be a candidate for more electron-rich ternary compounds like ZrMoP. The synthesis and single-crystal structure determination of $Hf_{1.06}Mo_{0.94}P$ proved our prediction. Analysis of the electronic DOS revealed that differences in homonuclear and heteronuclear metal−metal bonding account for these structural preferences. For vec less than 14 per formula unit, the Cu_2Sb structure type is predicted to be preferred, but a strong metal−phosphorus charge-transfer component may limit these phosphides to alkali metal systems in order to establish a stable configuration for the transition metal.

Table 6. Atomic Parameters Used in the Extended Hückel Calculations[a]

atom	orbital	H_{ii}	ζ_1	C_1	ζ_2	C_2
P	3s	−18.60	1.88			
	3p	−12.50	1.63			
Zr	4s	−8.41	1.82			
	4p	−4.81	1.78			
	3d	−8.41	3.84	0.6213	1.51	0.5798
Nb	4s	−8.58	1.89			
	4p	−4.76	1.85			
	3d	−9.22	4.08	0.6401	1.64	0.5516

[a] Double-ζ functions are used for the transition metals.

Acknowledgment. J.C. thanks Prof. H. F. Franzen for suggestions and Proj. R. A. Jacobson for the use of a Rigaku AFC6 rotating-anode single-crystal diffractometer. This project was supported both by the Office of the Basic Energy Sciences, Materials Science Division, U.S. Department of Energy, under Contract No. W-7405-Eng-82 and by the donors of the Petroleum Research Fund, administered by the American Chemical Society.

Appendix

All electronic structure calculations were of the extended Hückel tight-binding type.[20] DOS and COOP curves were evaluated using special **k**-point sets,[21] and tight-binding overlaps were included within two neighboring unit cells along every translation vector. Table 6 lists atomic orbital parameters, i.e., energies and exponents, used in our calculations. Orbital parameters for P were taken from standard sources.[22] The orbital energies of Zr and Nb were corrected for charge transfer using a charge iteration procedure.[23]

Supplementary Material Available: Tables S1−S4, listing complete crystallographic data, positional, isotropic, and anisotropic displacement parameters, and bond distances (3 pages). Ordering information is given on any current masthead page.

IC941296A

(19) Achenbach, G.; Schuster, H. U. *Z. Anorg. Allg. Chem.* **1981**, *475*, 9.
(20) Whangbo, M.-H.; Hoffmann, R.; Woodward, R. B. *Proc. R. Soc. London* **1979**, *A366*, 23.
(21) Chadi, D. J.; Cohen, M. L. *Phys. Rev. B* **1973**, *8*, 5747.
(22) (a) Clementi, E.; Roetti, C. *At. Data Nucl. Data Tables* **1974**, *14*, 177. (b) Herman, F.; Skillman, S. *Atomic Structure Calculations*; Prentice-Hall: Englewood Cliffs, NJ, 1963.
(23) (a) Ballhausen, C. J.; Gray, H. B. *Molecular Orbital Theory*; W. A. Benjamin, Inc.: New York, 1964. (b) Baranovskii, V. I.; Nikolskii, A. B. *Teor. Eksp. Khim.* **1967**, *3*, 527.